

# Mesoscopic modelling of heterogeneous boundary conditions for microchannel flows

By R. BENZI<sup>1</sup>, L. BIFERALE<sup>1</sup>, M. SBRAGAGLIA<sup>1</sup>,  
S. SUCCI<sup>2</sup> AND F. TOSCHI<sup>2,3</sup>

<sup>1</sup>Dipartimento di Fisica, Università ‘Tor Vergata’, and INFN,  
Via della Ricerca Scientifica 1, I-00133 Roma, Italy

<sup>2</sup>CNR, IAC, Viale del Policlinico 137, I-00161 Roma, Italy

<sup>3</sup>INFN, Via Paradiso 12, I-43100 Ferrara, Italy

(Received 22 February 2005 and in revised form 26 July 2005)

We present a mesoscopic model of the fluid–wall interactions for flows in microchannel geometries. We define a suitable implementation of the boundary conditions for a discrete version of the Boltzmann equations describing a wall-bounded single-phase fluid. We distinguish different slippage properties on the surface by introducing a slip function, defining the local degree of slip for hydrodynamical fields at the boundaries. The slip function plays the role of a renormalizing factor which incorporates, with some degree of arbitrariness, the microscopic effects on the mesoscopic description. We discuss the mesoscopic slip properties in terms of slip length, slip velocity, pressure drop reduction (drag reduction), and mass flow rate in microchannels as a function of the degree of slippage and of its spatial distribution and localization, the latter parameter mimicking the degree of roughness of the ultra-hydrophobic material in real experiments. We also discuss the increment of the slip length in the transition regime, i.e. at  $O(1)$  Knudsen numbers.

Finally, we compare our results with molecular dynamics investigations of the dependence of the slip length on the mean channel pressure and local slip properties and with the experimental dependence of the pressure drop reduction on the percentage of hydrophobic material deposited on the surface.

---

## 1. Introduction

The physics of molecular interactions at fluid–solid interfaces is a very active research area with a significant impact on many emerging applications in materials; science, chemistry, micro/nanoengineering, biology and medicine, see Ho & Tai (1998), Gad-el’Hak (1999), Whitesides & Stroock (2001), Lion *et al.* (2003). As for most problems connected with surface effects, fluid–solid interactions become particularly important for micro- and nano-devices, whose physical behaviour is largely affected by high surface/volume ratios. Recently, owing to an ever-increasing interest in microfluidics and MEMS (micro-electromechanical system)-based devices, experimental capabilities to test and analyse such systems have undergone remarkable progress.

In this paper, we shall focus on flows in micro-channels, a subject which has recently become accessible to systematic experimental studies thanks to the developments of silicon technology and polymeric devices (see Whitesides & Stroock 2001; Karniadakis & Benskok 2002; Tabeling 2003, and references therein).

Classical hydrodynamics postulates that a fluid flowing over a solid wall sticks to the boundaries, i.e. the hydrodynamical field shares the same velocity of the surfaces, (Batchelor 1967; Massey 1989). This law, and its consequences, are verified at a macroscopic level, where the characteristic scales of the flow are much larger than the molecular sizes. The situation changes drastically at a microscopic level. Many experiments (Vinogradova 1999; Watanabe, Yanuar & Ugadawa 1999; Pit, Hervet & Leger 2000; Choi *et al.* 2003; Craig, Neto & Williams 2001; Zhu & Granick 2001, 2002; Bonnacurso *et al.* 2002, 2003; Cheng & Giordano 2002; Baudry *et al.* 2001; Tretheway & Meinhart 2002; Zhang, Zhu & Granick 2002; Vinogradova & Yabukov 2003; Maurer *et al.* 2004; Ou, Perot & Rothstein 2004) and numerical simulations using molecular dynamics (Thompson & Robbins 1989; Thompson & Robbins 1990; Bocquet & Barrat 1993; Thompson & Troian 1997; Barrat & Bocquet 1999*a,b*; Cieplak, Koplik & Banavar 2001; Priezjev, Darhuber & Troian 2004) have shown evidence that the solid–fluid interactions are strongly affected by the chemico-physical properties and by the roughness of the surface. For example, water flowing over a hydrophilic, hydrophobic or super-hydrophobic surface, may develop quite different flow profiles in micro-structures. One of the most relevant effect is the appearance of an effective slip velocity,  $V_s$ , at the boundary, which, in turn, may imply a reduction of the stress for a given kinematics, with a significant enhancement of the overall throughput (at a given pressure drop) (see Watanabe *et al.* 1999; Pit *et al.* 2000; Baudry *et al.* 2001; Craig *et al.* 2001; Zhu & Granick 2001, 2002; Bonnacurso *et al.* 2002; Cheng & Giordano 2002; Tretheway & Meinhart 2002; Choi *et al.* 2003; Vinogradova & Yabukov 2003). From the slip velocity, we define a slip length,  $L_s$ , as the distance from the wall where the linearly extrapolated velocity profile vanishes. The experimental and theoretical picture is still under active development. No clear systematic trend of the slip effect as a function of the chemico-physical components has been found to date. Slip lengths varying from hundreds of nm up to tens of  $\mu\text{m}$  have been reported in the literature. Moreover, controversial claims about the importance of the roughness of the surface and of the combined degree of roughness–hydrophobicity have been presented. In simple flows, roughness is expected to increase the energy exchange with the boundaries, inducing a corresponding decrease in the slippage. However, both increase and decrease of the slip length as a function of the surface roughness have been claimed in the literature (Zhu & Granick 2001, 2002; Bonnacurso *et al.* 2002, 2003). From a purely molecular point of view, a critical parameter governing the solid–liquid interface is the contact angle (wetting angle). Clean glass is highly hydrophilic, with an angle with water close to  $\theta = 0^\circ$  (perfect wetting). Ultra-hydrophobic surfaces have been obtained which prove capable of sustaining a contact angle with water as high as  $\theta = 177^\circ$ , a value at which water droplets are almost spherical on the surface (Chen *et al.* 1999; Fadeev & Carthy 1999).

Some authors proposed that the increase in the slippage might be due to a rarefaction of the flow close to the wall, a depleted water region or vapour layer should exist near a hydrophobic surface in contact with water (Sakurai *et al.* 1998; Lum, Chandler & Weeks 1999; Tyrrell & Attard 2001; Schwendel *et al.* 2003). Recent molecular dynamics simulations have also presented some evidence of a dewetting transition, leading to a strong increase of the slip length, below some capillarity pressure in microchannels with heterogeneous surfaces (Cottin-Bizonne *et al.* 2003, 2004). Most of the physical aspects must be assessed because of the dependence on many chemical and geometrical details.

From the numerical point of view, molecular dynamics (MD) is the standard tool to systematically investigate the problem (Boon & Yip 1991; Frenkel & Smit

1995; Rapaport 1995). In MD, the solid–liquid and the liquid–liquid interactions are introduced by using Lennard–Jones type potential (with interaction energies and molecular diameters adjusted from experiments). By changing the interaction energies we can tune the surface tension and, consequently, the contact angles. MD also offers the possibility of modelling the boundary geometries and roughness with a high degree of fidelity. The main limitation, however, is the modest range of space and especially time scales, which can be simulated at a reasonable computational time, typically a few nanoseconds (Koplik & Banavar 1991; Rapaport 1995).

The coupling between MD and hydrodynamic modes involves a huge gap of space and time scales. An attempt to reproduce MD simulations of heterogeneous microchannels with a continuum mechanical description based on Navier–Stokes equations and suitable hydrodynamic boundary conditions has been proposed (Cottin-Bizonne *et al.* 2003, 2004; Priezjev *et al.* 2004). Cottin-Bizonne *et al.* (2004) show that some of the results obtained by MD simulations of a microchannel with a grooved surface can be qualitatively reproduced using a Stokes equation for the incompressible flow, in combination with an heterogeneous boundary condition, linking the slip velocity parallel to a flat surface  $\mathbf{u}_{\parallel}(\mathbf{r})$  to the stress in the normal direction,  $\hat{n}$ :

$$\mathbf{u}_{\parallel}(\mathbf{r}) = b(\mathbf{r})\partial_n \mathbf{u}_{\parallel}(\mathbf{r}), \quad (1.1)$$

where  $b(\mathbf{r})$  is a position-dependent normalized slip length mimicking the heterogeneity of the microscopic level. The qualitative agreement with the results of MD simulations can be obtained by properly tuning the  $b(\mathbf{r})$  values. In particular, they show that the dewetting transition observed in MD simulations, for some values in the pressure–volume diagram, is equivalent to the assumption, at the hydrodynamic level, that the boundary surface is made up of alternating strips of free-shear (high slip length  $b(\mathbf{r})$ ) and wetting material (low slip length).

In this paper, we aim mainly at filling the gap between the microscopic description typical of MD, and the macroscopic level of the Navier–Stokes equations by using a mesoscopic model based on the Boltzmann equation. In particular, we will use a discrete model known as the lattice Boltzmann equation (LBE) with heterogeneous boundary conditions.

The boundary condition (1.1), Maxwell (1879), arises naturally in a power expansion of the Boltzmann equation in terms of the Knudsen number,

$$Kn = \lambda/L,$$

which is the ratio of the mean free path,  $\lambda$ , and a typical length of the channel,  $L$ . At first order in  $Kn$ , we obtain the Navier–Stokes equation with the Maxwell boundary conditions above (Cercignani & Daneri 1963; Hadjiconstatinou 2003).

However, recent experimental results cast some doubt on the validity of this construction above some critical value of the Knudsen number. Maurer *et al.* (2004) report that above  $Kn \sim 0.3 \pm 0.1$ , both helium and nitrogen exhibit a nonlinear dependence of the flow rate on  $Kn$  which cannot be explained by solving the Stokes equation with the first-order slip boundary condition (1.1). For those values of  $Kn$ , the flow is in the so-called *transition regime* and it has been shown that the coupling between hydrodynamic equations with a second-order boundary condition

$$\mathbf{u}_{\parallel}(\mathbf{r}) = b_1(\mathbf{r})\partial_n \mathbf{u}_{\parallel}(\mathbf{r}) + b_2(\mathbf{r})\partial_n^2 \mathbf{u}_{\parallel}(\mathbf{r}) \quad (1.2)$$

is more appropriate to fit the experimental data (Maurer *et al.* 2004). The definition of the mean free path for a dense liquid is not as straightforward as for an ideal gas, because of the existence of a quasi-ordered structure on distance of the order of a

few nanometres. However, using a practical definition of ‘effective’ mean free path from the connection between kinematic viscosity and the sound speed of the medium, we can give an estimate of it. For example, for dense water at room temperature, we obtain  $\lambda \sim 1$  nm. This leads to characteristic Knudsen numbers in the range of  $10^{-6} \div 10^{-4}$  for microchannels.

The purpose of our investigation is twofold. First, we aim to develop a model which allows a coarse-grained treatment of local effects close to the flow-surface region, without delving into the detailed molecule–molecule description typical of MD. Secondly, we wish to design a tool capable of describing fluid motion also beyond the linear Knudsen regime.

The underlying hope behind the present hydro-kinetic approach, is that the main features of the fluid–surface interactions can be rearranged into a suitable set of renormalized LBE boundary conditions. This implies that all details of the contact angle, the solid–fluid interaction length, the local microscopic degree of roughness, can, to some extent, be included within the local definition of effective accommodation factors governing the statistical interactions between the mesoscopic populations and the solid walls (Lavalée, Boon & Noullez 1991; Luo 1998; Succi 2002; Sbragaglia & Succi 2005; Zhu *et al.* 2005). In a more microscopic vein, we may also describe the interactions between solid–liquid and liquid–liquid populations using a mean-field multi-phase LBE description (see Shan & Chen 1993, 1994; Swift, Osborn & Yeomans 1995; Verberg & Ladd 2000; Verberg *et al.* 2004; Kwok 2003. Results based on these more sophisticated schemes will be reported in a forthcoming paper (Benzi *et al.* 2005).

The paper is organized as follows. In §2, we briefly revise the main ideas behind the lattice versions of the Boltzmann equations and we present a natural way to implement non-homogeneous slip and no-slip boundary conditions in the model. In §3, we discuss the hydrodynamic limit of the LBE previously introduced, with particular emphasis on the form of the hydrodynamic boundary conditions in the presence of slippage. In §4, we present the numerical results at various Knudsen and Reynolds numbers, as well as a function of the degree of slippage and localization. Whenever directly applicable, we compare the results obtained within our mesoscopic approach with (i) exact results in the limit of small Knudsen numbers obtained in the hydrodynamic formalism (Philip 1972*a, b*; Lauga & Stone 2003); (ii) results obtained with a microscopic approach using MD simulations (Cottin-Bizonne *et al.* 2004); and (iii) experimental results of microchannels with ultrahydrophobic surfaces (Onda *et al.* 1996; Bico, Marzolin & Quere 1999; Ou *et al.* 2004). Conclusions and discussion follow in §5. Technical details are given in the Appendices.

## 2. Lattice kinetic formulation

The Boltzmann equation describes the space–time evolution of the probability density  $f(\mathbf{r}, \mathbf{v}, t)$  of finding a particle at position  $\mathbf{r}$  with velocity  $\mathbf{v}$  at a given time  $t$ . This evolution is governed by the competition between free-particle motion and molecular collisions which promote relaxation toward a non-homogeneous equilibrium, whose distribution  $f^{eq}(\rho, \mathbf{u})$ , is the Maxwellian consistent with the local density,  $\rho(\mathbf{r})$ , and coarse grained velocity,  $\mathbf{u}(\mathbf{r})$ . The hydrodynamic variables are obtained as low-order moments of the velocity distributions. In fact, the hydrodynamic density and velocity are  $\rho(\mathbf{r}, t) = \int d\mathbf{v} f(\mathbf{r}, \mathbf{v})$ , and  $\mathbf{u}(\mathbf{r}, t) = \int d\mathbf{v} \mathbf{v} f(\mathbf{r}, \mathbf{v})$ , respectively. The Navier–Stokes equations for the hydrodynamic fields are recovered in the limit of small-Knudsen numbers using the Chapman–Enskog expansion (Cercignani 1991).

The Boltzmann equation lives in a six-dimensional phase-space and consequently its numerical solution is extremely demanding, and typically handled by stochastic methods, primarily direct simulation Monte Carlo (for a review see Bird 1998). However, in the last fifteen years, a very appealing alternative (for hydrodynamic purposes) has emerged in the form of lattice versions of the Boltzmann equations in which the velocity phase space is discretized in a minimal form, through a handful of properly chosen discrete speeds (of order 10 in two dimensions and 20 in three dimensions – see Appendix A for details).

This leads to the lattice Boltzmann equations (LBE) for the probability density,  $f_l(\mathbf{r}, t)$ , where  $\mathbf{r}$  runs over the discrete lattice, and the subscript  $l = 0, N - 1$  labels the  $N$  discrete velocity values allowed by the scheme,  $\mathbf{v} \in \{\mathbf{c}_0, \dots, \mathbf{c}_{N-1}\}$ , (Benzi, Succi & Vergassola 1992; Chen & Doolen 1998; McNamara & Zanetti 1998; Wolf-Gladrow 2000; Succi 2001). It is sufficient to retain a limited numbers of discretized velocities at each site to recover the Navier–Stokes equations in the hydrodynamic limit. In two dimensions, the nine-speed  $2DQ9$  model ( $N = 9$ ) is, in fact, one of the most used two-dimensional LBE schemes, owing to its enhanced stability (Karlin, Ferrante & Oettinger 1999). All three-dimensional simulations described in this paper are based on the the  $3DQ19$  scheme ( $N = 19$ ) (see figure A 1 for a graphical description of LBE velocities in two and three dimensions). For the sake of concreteness, we shall refer to the two-dimensional nine-speed  $2DQ9$  model, although the proposed analysis can be extended in full generality to any other discrete-speed model living on a regular lattice. We begin by considering the lattice Boltzmann equation in the following BGK approximation (Bhatnagar, Gross & Krook 1954):

$$f_l(\mathbf{r} + \mathbf{c}_l, t + 1) - f_l(\mathbf{r}, t) = -\frac{1}{\tau}(f_l(\mathbf{r}, t) - f_l^{(eq)}(\rho, \mathbf{u})) + F_l, \quad (2.1)$$

where we have assumed lattice units  $\delta_x = \delta_t = 1$ . In (2.1),  $\tau$  is the relaxation time to the local equilibrium, which is proportional to the Knudsen number. The explicit expression of the speed vectors,  $\mathbf{c}_l$ , of the lattice equilibrium distribution,  $f_l^{(eq)}(\rho, \mathbf{u})$  and of the forcing term  $F_l$  required to reproduce a constant pressure drop, are described in Appendix A. The hydrodynamic fields in the lattice version are expressed by:

$$\rho(\mathbf{r}) = \sum_l f_l(\mathbf{r}); \quad \rho(\mathbf{r})\mathbf{u}(\mathbf{r}) = \sum_l \mathbf{c}_l f_l(\mathbf{r}). \quad (2.2)$$

Boundary conditions for lattice Boltzmann simulations of microscopic flows have been the object of much investigation in recent years (Ansumali & Karlin 2002a; Lim *et al.* 2002; Niu, Shu & Chew 2004; Toschi & Succi 2005). In particular, we are interested in studying the evolution of the LBE in a microchannel with heterogeneous boundary conditions (H-LBE) – the simplest case being a sequence of two alternating strips with different slip properties, as depicted in figure 1. A general way of imposing the boundary conditions in the LBE is

$$f_{\bar{k}}(\mathbf{r}_w, t + 1) = \sum_{\bar{l}} B_{\bar{k}, \bar{l}}(\mathbf{r}_w) f_{\bar{l}}(\mathbf{r}_w, t), \quad (2.3)$$

where the matrix  $B_{\bar{k}, \bar{l}}$  is the discrete analogue of the boundary scattering kernel expressing the fluid-wall interactions. Here and in the following, we use the notation  $\mathbf{r}_w$  to indicate the generic spatial coordinate over the surface of the wall and the indices  $\bar{l}, \bar{k}$  label the subset of incoming and outgoing velocities, respectively. To guarantee

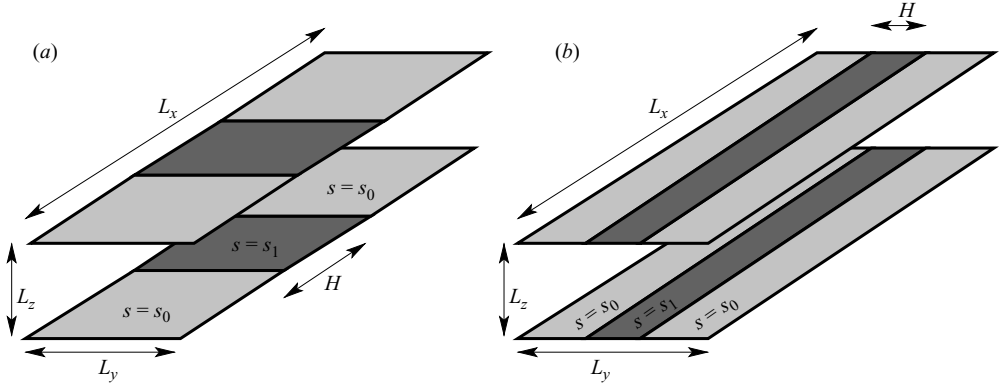


FIGURE 1. Typical geometry of the microchannel configuration. We have periodic boundary conditions along the streamwise,  $\hat{x}$ , and spanwise,  $\hat{y}$ , directions. The two rigid walls at  $z=0, L_z$  are covered by two strips of width  $H$  and  $L - H$ , where (a)  $L = L_x$  for transversal strips and (b)  $L = L_y$  for longitudinal strips. The two strips have different slippage properties identified by the values  $s_0$  and  $s_1$ . The ratio  $\xi = H/L$  identifies the fraction of hydrophobic material deposited on the surface. Typical sizes used in the LBE simulations are  $L_x = L_y = 64$  grid points and  $L_z = 84$  grid points. This would correspond, for example, for an ordinary gas at  $Kn = 10^{-3}$ , to a microchannel of height of the order of  $100 \mu\text{m}$ .

conservation of mass and normal momentum, the following sum-rule applies:

$$\sum_{\bar{k}} B_{\bar{k},\bar{l}}(\mathbf{r}_w) = 1. \quad (2.4)$$

On the assumption of fluid stationarity, we can drop the dependence on  $t$  and write:

$$f_{\bar{k}} = \sum_{\bar{l}} B_{\bar{k},\bar{l}}(\mathbf{r}_w) f_{\bar{l}}. \quad (2.5)$$

The simplest, non-trivial, application involves a *slip function*,  $s(\mathbf{r}_w)$ , representing the probability for a particle to slip forward (conversely,  $1 - s(\mathbf{r}_w)$  corresponds to the probability for the particle to be bounced back). If we focus, for example, on the north-wall boundary condition (see figure A 1), the boundary kernel, on the assumption of preserved density and zero normal component of the velocity field (2.4), takes the form :

$$\begin{pmatrix} f_7 \\ f_4 \\ f_8 \end{pmatrix} = \begin{pmatrix} 1 - s(\mathbf{r}_w) & 0 & s(\mathbf{r}_w) \\ 0 & 1 & 0 \\ s(\mathbf{r}_w) & 0 & 1 - s(\mathbf{r}_w) \end{pmatrix} \begin{pmatrix} f_5 \\ f_2 \\ f_6 \end{pmatrix}. \quad (2.6)$$

In this language, the usual no-slip boundary conditions are recovered in the limit  $s(\mathbf{r}_w) \rightarrow 0$  everywhere (incoming velocities are equal and opposite to the outgoing velocities), whereas the perfect free-shear profile is obtained with  $s(\mathbf{r}_w) \equiv 1$ . The formalism is sufficiently flexible to allow the study of both spatial inhomogeneity of a given hydrophobic material and/or the effects of different degrees of hydrophobicity at different spatial locations.

The above LBE scheme has already been successfully tested in the case of a homogeneous slippage  $s(\mathbf{r}_w) = s_0, \forall \mathbf{r}_w$  (Sbragaglia & Succi 2005). In that case, it has been shown (see Appendix B) that the LBE scheme converges to an hydrodynamic

limit with the slip boundary condition

$$\mathbf{u}_{\parallel} = A Kn |\partial_n \mathbf{u}_{\parallel}| + B Kn^2 |\partial_n^2 \mathbf{u}_{\parallel}|, \quad (2.7)$$

where the parameters  $A, B$  can be tuned by changing the degree of slippage,  $s_0$  and the external forcing. In this case, the LBE reproduces the analytical prediction for the slip length, obtained by assuming the existence of a Poiseuille velocity profile and, with a suitable choice of  $A, B$  in (2.7), we can show that the model is also able to fit the experimental nonlinear dependencies on the Knudsen number observed in Maurer *et al.* (2004) for nitrogen and helium.

### 3. Hydrodynamic limit

To begin with, we wish to analyse the hydrodynamic limit,  $Kn \rightarrow 0$ , of the previous LBE models with non-homogeneous boundary conditions, as dictated by the space-dependent profile of the slip function,  $s(\mathbf{r}_w)$ , at the walls. For the sake of simplicity, we shall confine our attention to the continuum limit of zero lattice spacing and time increments,  $\delta_x = \delta_t \rightarrow 0$ . Starting from the discretized equations (2.1), we obtain for the continuum limit of the LBE:

$$\partial_t f_l + (\mathbf{c}_l \cdot \nabla) f_l = -\frac{1}{\tau} (f_l - f_l^{(eq)}) + F_l. \quad (3.1)$$

In the following, we are interested in the case of stationary time-independent solutions (small-Reynolds regime). For this purpose, we may formally write the solution of (3.1) by using the time-independent Green's function:

$$f_l(\mathbf{r}) = \sum_{n=0}^{\infty} (-1)^n (\tau (\mathbf{c}_l \cdot \nabla))^n [f_l^{(eq)}(\rho, \mathbf{u}) + \tau F_l]. \quad (3.2)$$

Notice that by defining  $\tau = KnL_z/c_s$  ( $c_s$  being the sound speed velocity), (3.2) can be interpreted as a formal solution in powers of the Knudsen number. By recalling the expression of the hydrodynamic fields (2.2), it can readily be checked that the boundary velocity can be expressed as a function of the velocity stress,  $\partial_i u_j$ , at the boundary itself. For the sake of simplicity, we report here only the first-order term (in the Knudsen and Mach numbers) of the expansion (see Appendix B):

$$\mathbf{u}_{\parallel}(\mathbf{r}_w) = Kn \left( \frac{c}{c_s} \right) \frac{s(\mathbf{r}_w)}{1 - s(\mathbf{r}_w)} |\partial_n \mathbf{u}_{\parallel}(\mathbf{r}_w)| + O(Kn^2), \quad (3.3)$$

which is a direct generalization of the result obtained for the case of homogeneous boundary conditions (2.7) with  $c$  the lattice velocity and  $c_s$  the sound speed velocity. The main difference is that, owing to the spatial dependence of the stress tensor along the wall, subtle nonlinear effects may be triggered by the spatial correlation between the slip function  $s(\mathbf{r}_w)$  and the stress at the wall. Let us make a short digression on the LBE potential and limitations. In order to clarify the range of applications of the method, let us estimate the typical parameters necessary to simulate a microchannel of height,  $D = 100 \mu\text{m}$ , filled with water,  $\nu_{H_2O} = 10^{-2} \text{cm}^2 \text{s}^{-1}$ , or with air,  $\nu_{air} = 1.510^{-1} \text{cm}^2 \text{s}^{-1}$ . Considering that the mean free path is  $\lambda_{H_2O} \sim 1 \text{nm}$  and  $\lambda_{air} \sim 0.1 \mu\text{m}$ , we obtain the following Knudsen numbers for the two flows,  $Kn_{H_2O} \sim 10^{-5}$  and  $Kn_{air} \sim 10^{-3}$ . With  $L_z = 100$  grid points for the discretization of the microchannel height, we have  $\delta_x = D/L_z = 1 \mu\text{m}$ . The relation between the kinematic viscosity and the grid lattice spacing and time increments is readily derived starting from the expression of the kinematic viscosity in physical units:  $\nu = C_s^2 \delta_t (\tau - 1/2)$ ,

where the factor  $1/2$  comes from the Lattice discretization and  $C_s$  is the sound speed in physical units, namely  $10^3 \text{ m s}^{-1}$  and  $3 \times 10^2 \text{ m s}^{-1}$  for water and air, respectively. In lattice units, we have  $C_s = c_s(\delta_x/\delta_t)$ , so that  $\nu = ((\tau - 1/2)3\delta_x^2/\delta_t)$ , where  $c_s^2 = 1/3$ . As a result, the relaxation times in the two cases can be estimated as follows,  $(\tau_{\text{H}_2\text{O}} - 1/2) \sim 10^{-3}$  and  $(\tau_{\text{air}} - 1/2) \sim 10^{-2}$ . Since the inviscid limit  $\nu \rightarrow 0$  is singular, the value of  $\tau$  cannot be taken arbitrarily close to  $1/2$  because of numerical instability (it should be observed that, for  $1/2 < \tau < 1$ , the discrete distribution  $f_i$  is no longer guaranteed to be positive definite (Luo & Lallemand 2000; Boghosian *et al.* 2001; Ansumali & Karlin 2002*b*; Luo 2002). Actual practice shows that the instability threshold is reached for  $(\tau - 1/2) \sim 10^{-3}$ . Therefore, in order to reach microchannel height of the order of  $100 \mu\text{m}$  for water, we would need much larger numerical resolution (see also discussion in §4.1)

The hydrodynamic equations of motion in the stationary case are:

$$\left. \begin{aligned} (\mathbf{u} \cdot \nabla)\mathbf{u} &= -\frac{\nabla P}{\rho} + \frac{1}{\rho} \nabla \cdot (\nu \rho \nabla \mathbf{u}), \\ \nabla \cdot (\rho \mathbf{u}) &= 0, \\ \mathbf{u}_{\parallel}(\mathbf{r}_w) &= Kn \left( \frac{c}{c_s} \right) \frac{s(\mathbf{r}_w)}{1 - s(\mathbf{r}_w)} |\partial_n \mathbf{u}_{\parallel}(\mathbf{r}_w)| + O(Kn^2), \\ \mathbf{u}_{\perp}(\mathbf{r}_w) &= 0, \end{aligned} \right\} \quad (3.4)$$

where  $\nabla P$  contains both the imposed mean pressure drop,  $\mathbf{F}$ , and the fluid pressure fluctuations. In the limit of small Mach numbers ( $\Delta\rho/\rho \ll 1$ ) we may take a constant density  $\rho = 1$ . Notice that in this limit, the incompressibility constraint  $\nabla \cdot \mathbf{u} = 0$  imposes that any nonhomogeneity of  $\mathbf{u}_{\parallel}$  along the wall-parallel direction must be compensated by an equal and opposite gradient of the normal velocity  $\mathbf{u}_{\perp}$ . This implies that the local velocity profile cannot be unidirectional everywhere ( $\mathbf{u}_{\perp} = 0$ ).

In (3.3), the local slip properties depend both on Knudsen (linearly for small  $Kn$ ) and on the boundary conditions, via the  $s(\mathbf{r}_w)$  function. The former stems from the explicit dependence of the viscosity on  $Kn$  via the definition,  $\nu = C_s L_z Kn$ , and can be regarded as a ‘bulk’ property, independent of the boundary conditions. As to the latter, it is important to notice that, in line with Maxwell’s calculation for an ideal gas, for intermediate values in the range  $0 < s < 1$ , the slip length vanishes in the limit of zero Knudsen number. We wish to emphasize that, according to the mesoscopic spirit of the present approach, it is the combined effect of a non-zero Knudsen and  $0 < s < 1$  which is meant to mimic the slip effects due to unresolved molecular interactions. For perfect slippage,  $s(\mathbf{r}_w) = 1$ , the boundary conditions (3.3) must be read as  $(1 - s)u_{\parallel} \propto \partial_n u_{\parallel}$ , meaning that second-order terms in the Knudsen number can no longer be ignored (see also (B5)). In the small-Knudsen regime, we recover a free-shear condition  $\partial_n \mathbf{u}_{\parallel}(\mathbf{r}_w) = 0$ , plus corrections  $O(Kn)$ . Therefore, for the case of a periodic array of alternating strips with  $s(\mathbf{r}_w) = 0$  or  $s(\mathbf{r}_w) = 1$  only, as in figure 1, we expect global slip properties almost independent of  $Kn$  in the small  $Kn$  limit.

In order to assess the effects of the slip on the global quantities, it is useful to define the mean profile,  $\langle \mathbf{u}(z) \rangle$ . Let us consider for instance the geometry depicted in figure 1, where the direction perpendicular to the walls is denoted by  $\hat{z}$ . We define a homogeneous mean profile as:

$$\langle \mathbf{u}(z) \rangle = \frac{1}{S} \int \mathbf{u}(\mathbf{r}) \, dx \, dy, \quad (3.5)$$

where  $\langle \dots \rangle$  stands for averaging over a plane parallel to the boundary surface,  $S$ . Even though the local velocity does not reproduce a Poiseuille profile, it can be shown

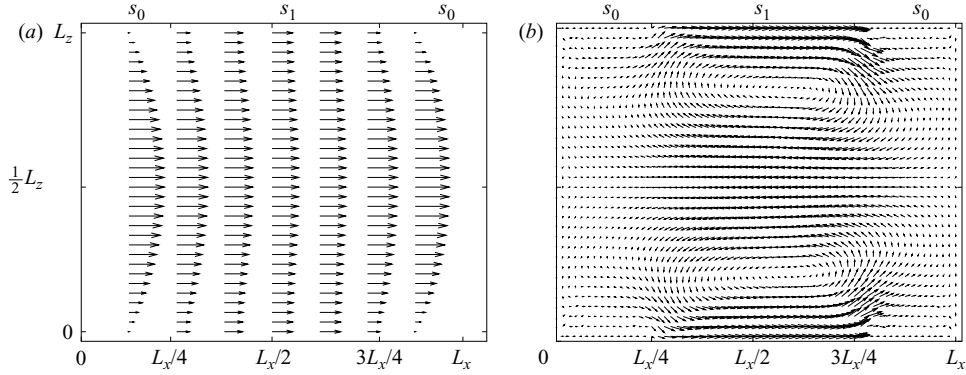


FIGURE 2. Results in the plane  $y = L_y/2$  along the channel measured in the transversal strip configuration (see figure 1a). (a) The velocity profile. Notice that the pure inlet Poiseuille flow becomes an almost perfect shear-free profile in the region with  $s_1 = 1$ . (b) Highlights the local differences between the pure Poiseuille flow and the measured profiles, showing the result for  $(\mathbf{u}_x(\mathbf{r}) - \mathbf{u}_x^{pois}(\mathbf{r}))$ . Notice the recirculation area, entering deep in the channel bulk, produced by the alternating slip and no-slip boundary conditions.

from (3.4) that in the case of periodic boundary conditions between inlet and outlet flows, the mean homogeneous profile (3.5) cannot develop nonlinear stresses, namely:

$$\langle \mathbf{u}(z) \rangle = u_{pois}(z) + u_{slip}, \quad (3.6)$$

with the notable fact that a slip velocity may appear at the boundary. In (3.6),  $u_{pois}(z)$  stands for the Poiseuille parabolic profile with zero velocity at the boundary. A first set of qualitative results are plotted in figure 2, where the local velocity profiles and the difference between the observed velocities and the standard no-slip Poiseuille flow are shown.

From (3.6), we may define a macroscopic, global slip length, as the distance away from the wall at which the linearly extrapolated slip profile (3.6) vanishes:

$$L_s = \frac{u_{slip}}{|\partial_z u_{pois}(z_w)|}, \quad (3.7)$$

where  $|\partial_z u_{pois}(z_w)|$  is the Poiseuille stress evaluated at the wall. Similarly, we may define the *mass flow rate* gain  $G$  as

$$G \equiv \frac{\Phi_s}{\Phi_p} = \left( 1 + \frac{6L_s}{L_z} \right), \quad (3.8)$$

$\Phi_s = \int u_x(\mathbf{r}) dy dz$  being the actual mass flow rate and  $\Phi_p$  the Poiseuille mass flow rate for our configuration:

$$\Phi_p = \left( -\frac{dP}{dx} \right) \frac{L_z^3 L_y}{12\mu}, \quad (3.9)$$

with  $\mu$  the dynamic viscosity of the fluid. In terms of these quantities, we can also define the pressure drop reduction,

$$\Pi = \frac{\Delta P_{no-slip} - \Delta P}{\Delta P_{no-slip}}, \quad (3.10)$$

which is defined as the gain with respect to the pressure drop corresponding to a non-slip channel with the same overall throughput,  $\Phi_s$ . The pressure drop reduction,  $\Pi$ , is usually interpreted as an effective *drag reduction* induced by the slippage.

#### 4. Numerical results

Next, we present the numerical results obtained from the H-LBE model by changing the spatial distribution and intensity of the slip function at the boundaries. We shall also address dependencies of the slip flow on the Knudsen and Reynolds numbers.

We begin by investigating the dependency of the macroscopic slip length,  $L_s$ , and the average mass flow rate through the channel, on the total amount of *slip material* deposited on the surface. The natural control parameter for investigating this issue is the average of the slip function on the boundary wall:

$$s_{av} = \langle s(\mathbf{r}_w) \rangle = \frac{1}{S} \int s(\mathbf{r}_w) dS \quad (4.1)$$

that is best interpreted as the *renormalized* effect of the total mass of hydrophobic material deposited on the surface, at the (unresolved) microscopic level.

Secondly, we also present results as a function of the non-homogeneity of the hydrophobic pattern. This non-homogeneity can be represented by the spatial variance of the slip function:

$$\Delta^2 = \langle (s(\mathbf{r}_w) - s_{av})^2 \rangle = \frac{1}{S} \int (s(\mathbf{r}_w) - \langle s \rangle)^2 dS. \quad (4.2)$$

In order to quantify the gain or the loss in the slip flow with respect to the homogeneous situation, we shall focus our attention mainly on the simplest non-trivial inhomogeneous boundary configurations sketched in figure 1.

This corresponds to a periodic array of two strips. In the first strip, of length  $H$ , the slip coefficient is chosen as  $s(\mathbf{r}_w) = s_1$ . In the second strip (of length  $L - H$ ), we impose  $s(\mathbf{r}_w) = s_0$ . We distinguish the two cases when the strips are oriented longitudinally or transversally to the mean flow. In these configurations, the total mass  $s_{av}$  is given by:

$$s_{av} = \xi s_1 + (1 - \xi) s_0,$$

and the degree of non-homogeneity by:

$$\Delta^2 = \xi(1 - \xi)(s_1 - s_0)^2.$$

By choosing (without loss of generality)  $s_1 > s_0$ , in this configuration the quantity  $\xi = H/L$  is a natural measure of the localization of the slip effect. This geometry allows us to compare our results with some analytical, numerical and experimental results for the small Knudsen regime and also to extend the study to the *transition regime*. In §4.3, we shall also present results with slightly more complex boundary conditions, namely for the case of a bi-periodic pattern of alternating slip and no-slip boundary conditions.

##### 4.1. Exact results and Knudsen effects

As a validation test, we first check whether our model can reproduce some of the existing results concerning the slip properties of hydrodynamic systems with boundaries consisting of alternating strips of zero-slip and infinite-slip lengths.

Philip (1972a) analysed this situation using the Navier–Stokes equations for the case of a cylinder with boundaries made up of alternating longitudinal strips of perfect-slip and no-slip. This author obtained the following exact result:

$$\ell_s^{long} \equiv \frac{L_s}{L_y} = \frac{1}{\pi} \log(1/\cos(\pi\xi/2)), \quad (4.3)$$

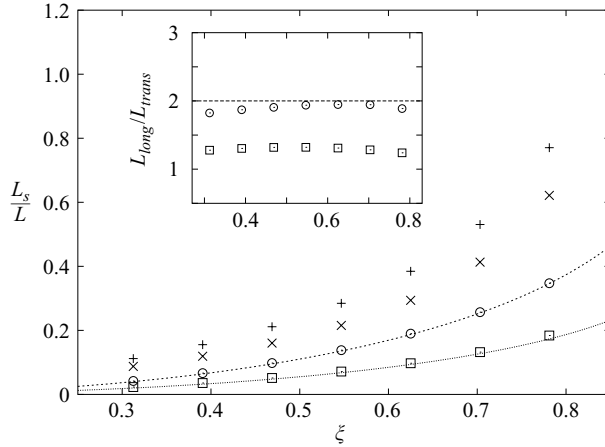


FIGURE 3. Normalized slip length for transversal and longitudinal strips with  $s_1 = 1$ ,  $s_0 = 0$ . We plot the normalized slip length as a function of the slip percentage  $\xi$ . The system's dimensions are those of figure 1. A first set of LBE simulations is carried out at small Knudsen number,  $Kn = 1 \times 10^{-3}$  for transversal ( $\square$ ) and longitudinal strips ( $\circ$ ). These results are compared with the analytical estimates of Philip (1972a) (dashed line) and Lauga & Stone (2003) (solid line). Notice the excellent agreement with the analytical results in the hydrodynamic limit. Another set of simulations is carried out with much larger Knudsen number,  $Kn = 5 \times 10^{-2}$  to highlight the effect of rarefaction on the system for both transversal ( $\times$ ) and longitudinal ( $+$ ) strips. In the inset, we show the ratio between the slip lengths for parallel and longitudinal strips for  $Kn = 1 \times 10^{-3}$  ( $\circ$ ) and  $Kn = 5 \times 10^{-2}$  ( $\square$ ). Here we notice that by increasing the Knudsen number, the orientation of the strip region with respect to the mean flow becomes less important.

where  $\xi$  is the fraction of the plate where the slip length is infinite and where we have defined  $\ell_s^{long}$  as the normalized (to the pattern dimension) macroscopic slip length.

Notice that the right-hand side of (4.3) is independent of the radius of the cylinder, and therefore Philip's result is directly applicable to our geometry of figure 1, in the limit of small Knudsen numbers. Lauga & Stone (2003) analysed the same situation with the only variant being the use of transversal rather than longitudinal strips. In the limit of a cylinder with infinite radius (plane wall boundaries), their result for the normalized slip length can be written as:

$$\ell_s^{trans} \equiv \frac{L_s}{L_x} = \frac{1}{2\pi} \log(1/\cos(\pi\xi/2)). \quad (4.4)$$

In our language, local infinite (zero) slip lengths can be obtained by choosing  $s_1 = 1$  ( $s_0 = 0$ ). A consistency check for our mesoscopic H-LBE model is to reproduce the hydrodynamic limits studied in the aforementioned papers, in the limit of small Knudsen numbers and large channel aspect ratio,  $L_z/L_x$ .

To this purpose, we performed a direct numerical simulation of the H-LBE model for a channel with square cross-section,  $L_x = L_y$ , and different heights,  $L_z$ . For small and fixed Knudsen number, by increasing the aspect ratio  $L_z/L_x$  at fixed channel length,  $L_x$ , the previous hydrodynamic limits are attained and the normalized slip lengths  $\ell_s^{trans}$ ,  $\ell_s^{long}$  are independent of  $L_z$ . In figure 3, we present the results obtained for both longitudinal and transversal strips compared with the analytical predictions (4.3)–(4.4) for a given channel aspect ratio.

The result (see figure 3) shows that the analytical hydrodynamic results are reproduced well by our mesoscopic model. Moreover, we can go beyond the hydrodynamical

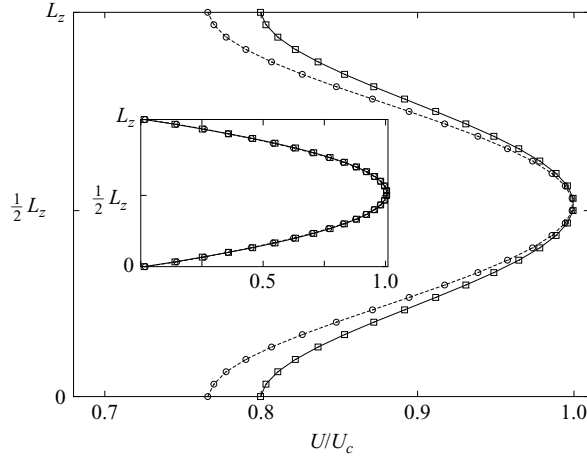


FIGURE 4. Local velocity profile in the middle of a slip strip (the one with  $s_1 = 1$ ) for transversal strips in the geometry depicted in figure 1. We plot the velocity in the streamwise direction as a function of the height  $z$  for two different Reynolds numbers  $Re \sim 4.5$  ( $\square$ ), and  $Re \sim 9.5$  ( $\circ$ ). The  $Re$  numbers are estimated as the ratio between the centre channel velocity of the integral profile and the sound speed velocity  $c_s$ . Both velocity fields are normalized with the centre channel velocity. The Knudsen numbers are  $Kn = 0.01$  and  $0.005$ , respectively. Inset: the same, but in the middle of a no-slip strip ( $s_0 = 0$ ).

limit studied by Philip (1972*a, b*) and Lauga & Stone (2003), and investigate the effect of larger Knudsen numbers on these configurations, both in the near-hydrodynamic and in the transition regimes observed in the experiments (Maurer *et al.* 2004). The result (see figure 3) is that an increase of the Knudsen number leads to an increase of the slip length, without preserving the ratio between  $\ell_s^{long}$  and  $\ell_s^{trans}$  (see inset of figure 3).

These results can be explained by observing that upon increasing the Knudsen number, the ‘non-conductive’ strips which had zero-slip length in the hydrodynamic regime, acquire a non-zero slip, due to effects of order  $Kn^2$  in the boundary conditions (Sbragaglia & Succi 2005). Moreover, even the perfect-slip strips acquire an additional slip due to higher-order terms in the Knudsen number, as given in equation (B 5). Notice that at still relatively small Knudsen numbers,  $Kn = 0.05$ , a fairly substantial increase of the global slip length is observed, which may reach 60–80% of the typical pattern dimension for a percentage of the slipping surface  $\xi \sim 0.8$ .

Another interesting question concerns the dependency of the local velocity profile on the local slip properties with changing Reynolds and Knudsen numbers. We choose a transversal periodic array of strips with  $H = L_x/2$  and  $s_0 = 0$ ,  $s_1 = 1$  and look at the profiles in the middle of the region with  $s_1 = 1$  and in the middle of the region with  $s_0 = 0$ . The results (figure 4) clearly indicate a dependency on the Knudsen and Reynolds numbers only in the slip region. This is readily understood by observing that the Reynolds number is given by  $Re = Ma/Kn$ , so that, by fixing the Mach number and varying the Reynolds number, we also change the Knudsen number, thus affecting the local slip properties of the flow. The most interesting result here is the inversion of concavity for the local profile near the wall in the slip region: a clear indication of the departure from the parabolic shape of the Poiseuille flow.

Next, we check our method against experimental results and MD simulations.

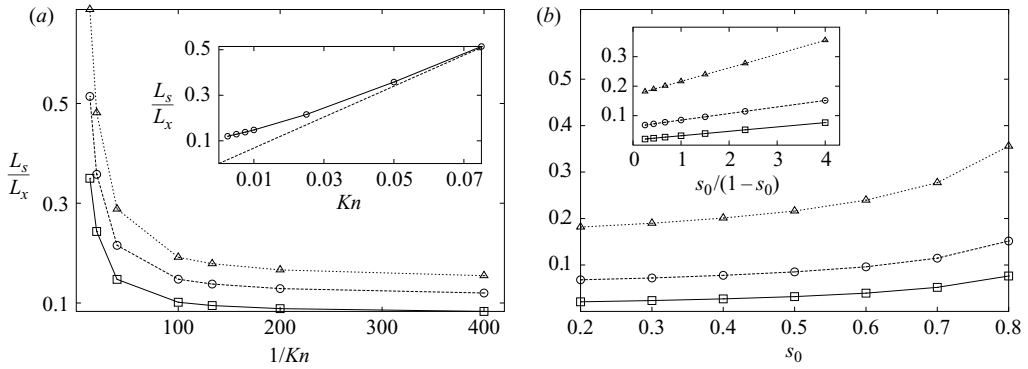


FIGURE 5. (a) Normalized transversal slip length,  $\ell_s^{trans} = L_s/L_x$ , as a function of the average pressure in the system (inverse of the Knudsen number) and for different values of the localization parameter:  $\xi = 0.58$  ( $\square$ ),  $\xi = 0.65$  ( $\circ$ ),  $\xi = 0.73$  ( $\triangle$ ). The values of  $s_0, s_1$  are kept fixed to  $s_0 = 0$  and  $s_1 = 1$ . This behaviour is qualitatively similar to that observed in MD simulations of microchannels with grooves, where the degree of slippage localization is governed by the width of the grooves (see Cottin-Bizonne *et al.* 2004). In the inset, we show the normalized slip length for the case  $\xi = 0.65$  as a function of  $Kn$  in order to highlight the deviation from the linear behaviour for small  $Kn$ . (b)  $\ell_s^{trans}$  as a function of the local degree of slippage  $s_0$  for different values of slippage localization,  $\xi = 0.25, 0.5, 0.75$  ( $\square, \circ, \triangle$ , respectively). In the inset, we show the dependency of the slip length,  $\ell_s^{trans}$ , on the microscopic slip properties,  $s_0/(1-s_0)$ , for the same values of  $\xi$ .

For example, in figure 5, we show the dependence of the transversal normalized slip length,  $\ell_s^{trans}$ , as a function of the inverse of the Knudsen number, i.e. as a function of the mean channel pressure, for different values of the localization parameter  $\xi$ . This is a direct comparison with the results in figure 6 of Cottin-Bizonne *et al.* (2004) where the evolution of the slip length as a function of the pressure in MD simulations of a channel with grooves of different width is shown. Also in that case, the slip length increases by either decreasing the pressure (increasing Knudsen) or increasing the groove width (increasing the region with infinite slip). The two behaviours are qualitatively similar, with a less pronounced slip length for our case because we show the case of transversal strips, while in figure 6 of Cottin-Bizonne *et al.* (2004) only the case of longitudinal grooves is presented. Again, we wish to emphasize that the linear dependence on  $Kn$  in the high- $Kn$  regime is a ‘bulk’ property ( $v \sim Kn$ ) which is triggered by surface effects, i.e.  $s > 0$  in our approach and by fine-tuning of fluid–wall potentials in MD simulations. In the inset of the same figure, we show the normalized slip length as a function of  $Kn$  superposed with the linear behaviour expected for large  $Kn$ . Notice that, even for strips with  $s = 0$  and  $s = 1$ , the system develops a finite slip length with an effective value of the slip function:  $0 < s_{eff} < 1$ , for large Knudsen. On the other hand, for small  $Kn$ , the behaviour is more tricky. For the case of strips with  $s_0 = 0$  and  $s_1 = 1$ , the behaviour clearly departs from the linear dependency (see inset of figure 5a, as it should according to the hydrodynamic limit discussed in Lauga & Stone (2003)). The case with  $s_0 > 0$  is shown in figure 5(b), where we plot  $\ell_s^{trans}$  at varying levels of slippage,  $s_0$ , of one of the two strips (the other being kept fixed to  $s_1 = 1$ ). This is meant to investigate the sensitivity of the macroscopic observable to the microscopic details. As can be seen, the change is never dramatic, at least for this configuration. In the inset of figure 5(b), we can see a linear dependency between  $\ell_s^{trans}$  and the local slip properties,  $s_0/(1-s_0)$ . For local slip properties we mean the local slip length as defined from the local boundary condition,

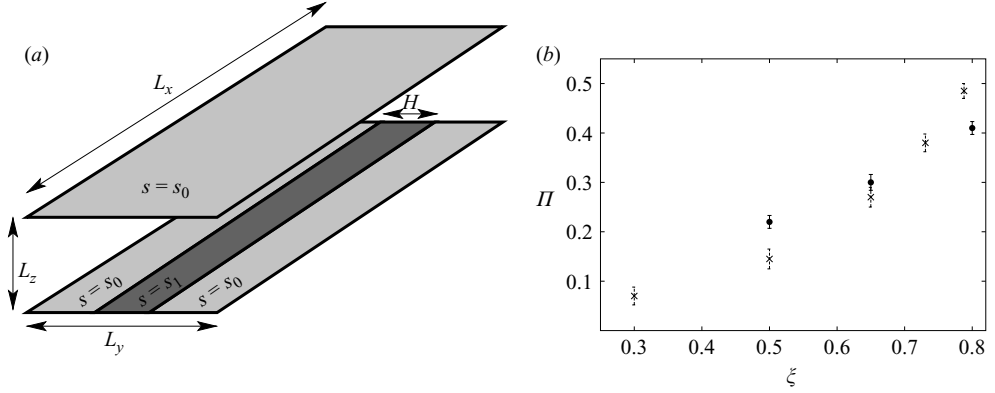


FIGURE 6. Results for the pressure drop reduction  $\Pi$  (3.10), as a function of the percentage of the free-slip area on the surface. The geometry is the same as that investigated experimentally in figure 15 of Ou *et al.* (2004) where a micro-channel with only one surface engraved with longitudinal strips with super-hydrophobic material is studied (a). Here we present the results from the experiments ( $\bullet$ ), superposed with our numerical simulations ( $\times$ ) obtained at  $Kn = 5 \times 10^{-4}$ . The numerical mesh is such as to mimic the same geometry of the experiment. The error bars in the LBE numerics represent the maximum variation obtained by fixing  $s_1 = 1$ , in the shear-free area, and changing  $s_0 \in [0.4, 0.65]$  in the normal surface.

$\mathbf{u}_{\parallel}(\mathbf{r}_w) \propto Kn(s(\mathbf{r}_w)/(1-s(\mathbf{r}_w)))|\partial_n \mathbf{u}_{\parallel}(\mathbf{r}_w)|$ . The same linear trend is observed in figure 12 of Cottin-Bizonne *et al.* (2004) for local scaling properties that are not too small, using a hydrodynamic model with suitable boundary conditions. Notice that while the behaviour proportional to  $Kn$  for large mean free path is expected, the results for small  $Kn$  and  $s_0 = 0, s_1 = 1$  deserve a delicate hydrodynamic interpretation (both in LBE approach or the pure hydrodynamic approach) which can eventually be accomplished by using averaged (global) quantities in the channel.

In figure 6, we present the same kind of plot as shown in the experimental investigation (see figure 15 of Ou *et al.* 2004). Here, we plot the pressure drop reduction,  $\Pi$ , in the microchannel as a function of the percentage,  $\xi$ , of the free slip area on the surface (super-hydrophobic material). We note a remarkable agreement with the experimental results over a wide range of  $\xi$ , i.e. the ratio between the regions with super-hydrophobic and normal material on the wall. The aspect ratios of the geometry are the same as in the experiment. Given the number of grid points used to discretize the channel height,  $L_z = 84$ , and the LBE relaxation time used,  $(\tau - 1/2) = 7 \times 10^{-2}$ , we may interpret the numerical experiment as describing a dense liquid like water in a channel height of  $\sim 2 \mu\text{m}$ , or an ordinary gas (air) in a channel height of  $\sim 800 \mu\text{m}$ . This corresponds to a Knudsen number of  $Kn = 5 \times 10^{-4}$ , which is slightly larger than that of the experiment,  $Kn_{exp} = 10^{-5}$ . In order to reach Knudsen numbers comparable with Ou *et al.* (2004) with water, we would require a much larger resolution  $L_z \sim 10^3$ . We may now tune the free parameters,  $s_0, s_1$  in order to match the experimental results for a given geometry, i.e. a given  $\xi$ . Once this is done, we may change the geometry and check whether the LBE scheme is flexible enough to follow the experimental trend. We have chosen  $s_1 = 1$  in the super-hydrophobic area, and we have varied  $s_0 \in [0.4, 0.65]$  for the normal material, to match the experiments at  $\xi = 0.65$ . In figure 6, we show that the LBE results indeed exhibit the same trend as the experiments as a function of  $\xi$ . Overall, there is a small dependence of  $\Pi$  on the unknown value of  $s_0$ , at least in the range considered, as already shown by the data presented in figure 5. Once the correct values of  $s_1$  and  $s_0$ , able to reproduce the

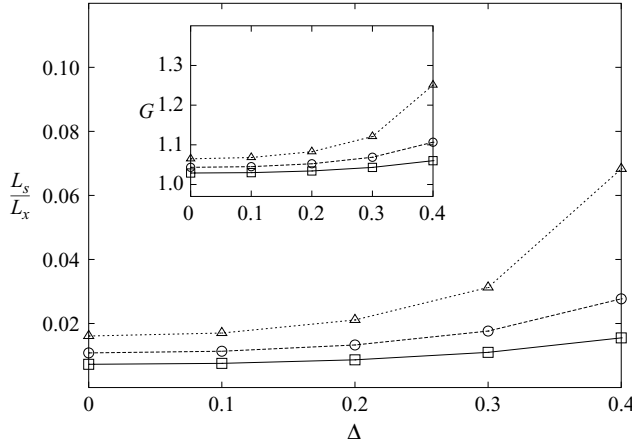


FIGURE 7. Normalized transversal slip length,  $\ell_s^{trans} = L_s/L_x$ , for boundary conditions as in figure 1 with  $s_1 = s_{av} + \Delta$  in a fraction  $\xi = H/L_x = 1/2$  and  $s_0 = s_{av} - \Delta$  in the other. The Knudsen number is  $Kn = 0.001$ . We plot the normalized slip length as a function of the heterogeneity parameter  $\Delta$  and the following values of  $s_{av}$  are considered:  $s_{av} = 0.4$  (□),  $s_{av} = 0.5$  (○),  $s_{av} = 0.6$  (△). Inset: same trends as the main body, but for the mass flow rate gain  $G$ .

experimental results, are identified, we can use the present LBE method to predict and extend the outcomes of other experiments with different geometries and/or distributions of the same hydrophobic material on the surface.

#### 4.2. Effects of heterogeneity and of localization

As a next step, we address of the effect of the roughness, the total mass of the hydrophobic material, and the localization over the surface.

To this purpose, we choose a transversal configuration where  $H = L_x/2$  (fixed localization,  $\xi = 0.5$ ) and

$$s_0 = s_{av} + \Delta, \quad s_1 = s_{av} - \Delta,$$

thus yielding  $\langle s \rangle = s_{av}$  for any degree of heterogeneity,  $\Delta$ .

We then look, for a given  $s_{av}$ , at how the slip properties of the system respond to changes in the excursion,  $\Delta$ , at fixed localization  $\xi$ . The results for the normalized transversal slip length,  $\ell_s^{trans}$ , and the mass flow rate gain, are presented in figure 7. Both the slip length and the mass flow rate increase by increasing  $\Delta$ . Notice that we can easily reach slip lengths which are of the order of 10 % of the channel pattern dimension by increasing the heterogeneity at fixed total mass of slip material deposited on the surface. Similarly, the mass flow rate gain,  $G$ , is increased in the order of 20–30 % with respect to the Poiseuille flow. In other words, the best throughput is obtained by increasing the inhomogeneity of the slippage material deposited on the surface (experimentally this means keeping the region covered by hydrophobic molecules as segregated as possible from the region covered with hydrophilic molecules).

Another possible way to compute the slippage effects is to analyse the slippage at fixed total mass of hydrophobic material, varying both the localization and the heterogeneity. To this purpose, we choose again a transversal configuration where we fix the total mass  $s_{av}$  and we choose  $s_1 = s_{av}/\xi$ ,  $s_0 = 0$ ,  $\xi = H/L_x$  being the degree of localization associated with a given heterogeneity. The result (figure 8) is that the

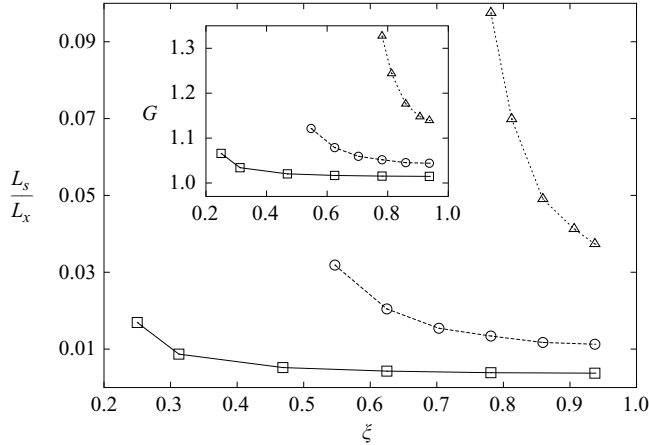


FIGURE 8. Normalized transversal slip length,  $\ell_s^{trans} = L_s/L_x$ , for boundary conditions of transversal strips as in figure 1 with  $s_1 = s_{av}/\xi$  in a fraction  $\xi$  and  $s_0 = 0$  in the other. The Knudsen number is  $Kn = 0.001$ . We plot the normalized slip length as a function of the localization parameter  $\xi$  for the following values of  $s_{av}$ :  $s_{av} = 0.25$  ( $\square$ ),  $s_{av} = 0.5$  ( $\circ$ ),  $s_{av} = 0.75$  ( $\triangle$ ). Inset: same trends of the main body, but for the mass flow rate gain  $G$ .

slippage is greater as the degree of localization, and, consequently, of the roughness, is increased.

### 4.3. Mean field approach and beyond

Let us develop out a mean field approach which is able to reproduce the qualitative trends observed so far in the case when the local slippage is not too high ( $s < 1$ ). In the boundary condition (3.3) there is a coupling between the local velocity field and the stresses at the wall. Obviously, the averaged slip length depends both on  $s(\mathbf{r}_w)$  and on the stresses.

In order to highlight the effect of the slip function on the mean quantities, as a first approximation, we can leave the wall stress fixed at its Poiseuille value, and work only on the properties of  $s(\mathbf{r}_w)$ , namely:

$$\langle u_{slip} \rangle \sim \left\langle \frac{s}{1-s} \right\rangle. \tag{4.5}$$

For the configuration analysed so far, without loss of generality we define:

$$\delta = \frac{s_1 - s_0}{2}, \quad s_+ = \frac{s_0 + s_1}{2},$$

and write the averaged slip properties  $\langle s/(1-s) \rangle$  as a function of  $\delta$  and  $s_+$ :

$$\left\langle \frac{s}{1-s} \right\rangle = p_0 \frac{s_0}{1-s_0} + p_1 \frac{s_1}{1-s_1} = p_0 \frac{s_+ - \delta}{1-s_+ + \delta} + p_1 \frac{s_+ + \delta}{1-s_+ - \delta}, \tag{4.6}$$

where  $p_1, p_0 = 1 - p_1$  are the percentages of the surface associated with slip and no-slip areas, respectively. Making use of Taylor expansion up to second order in  $\delta$  we obtain:

$$\left\langle \frac{s}{1-s} \right\rangle \approx \frac{s_+}{1-s_+} + \frac{\delta}{(1-s_+)^2} (p_1 - p_0) + \frac{\delta^2}{(1-s_+)^3}. \tag{4.7}$$

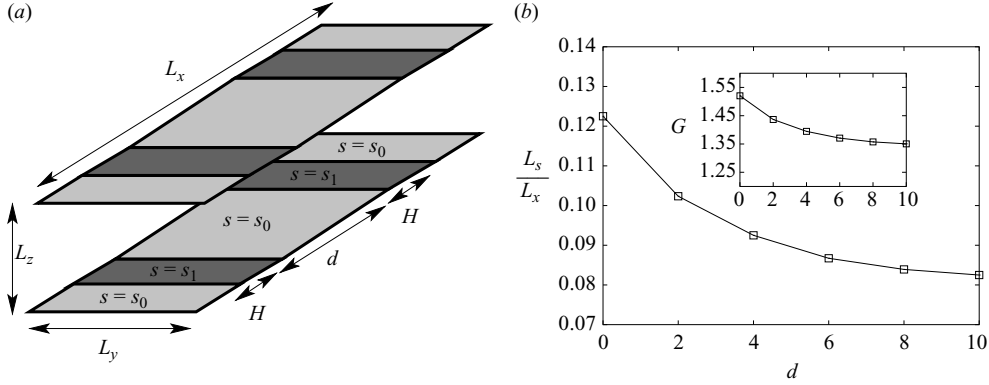


FIGURE 9. (a) The configuration with a transversal bi-strip structure at the walls. The total boundary lengths are  $L_x, L_y$  (stream, span). The slip coefficient is chosen as  $s_1 = 1$  in two strip of length  $H$  and  $s_0 = 0$  in the others. The distance between the two strips is  $d$ . Periodic boundary conditions are always assumed in the spanwise and streamwise directions. (b) Results for the slip length and the mass flow-rate gain (inset) as a function of the distance  $d$  (in lattice units) between the two free-shear ( $s = s_1$ ) strips of width  $H = 20$  (in lattice units). All the other parameters,  $L_x = L_y = 64, L_z = 84, Kn = 1 \times 10^{-3}$  are fixed.

Since  $p_1 = H/L_x = \xi$  and  $p_0 + p_1 = 1$ , we finally obtain:

$$\left\langle \frac{s}{1-s} \right\rangle \approx \frac{s_+}{1-s_+} + \frac{\delta(2\xi - 1)(1-s_+) + \delta^2}{(1-s_+)^3}. \quad (4.8)$$

First, in our case of a fixed localization, by setting  $\xi = 1/2$  we have  $s_+ = s_{av}$ ,  $\delta = \Delta$  and we obtain:

$$\left\langle \frac{s}{1-s} \right\rangle \approx \frac{s_{av}}{1-s_{av}} + \frac{\Delta^2}{(1-s_{av})^3}, \quad (4.9)$$

that results in a greater slippage when the heterogeneity  $\Delta$  is increased. However, note that (4.8) has its leading order in the term  $2\xi - 1$ , and it is the sign of this term that governs the dependence of the effective slippage in the most general case ( $\xi \neq 1/2$ ).

Secondly, if we choose  $s_1 = s_{av}/\xi$  and  $s_0 = 0$ , as for the case with fixed total mass, we obtain  $\delta = s_{av}/2\xi$  and  $s_+ = s_{av}/2\xi$ . This results in

$$\left\langle \frac{s}{1-s} \right\rangle \approx \frac{s_{av}}{(2\xi - s_{av})} + \frac{s_{av}(4\xi^2 - 2\xi)(2\xi - s_{av}) + 2\xi s_{av}^2}{(2\xi - s_{av})^3}, \quad (4.10)$$

that, as a function of the localization  $\xi$ , yields a qualitative agreement with our analysis, supporting the idea that the effect of slippage is greater when slip properties are localized.

It should be appreciated that the mean field approach discussed above is not exhaustive. In fact, we can design an experiment with the boundary configuration sketched in figure 9, and investigate the total slippage as a function of the distance,  $d$ , between the strips. For this geometry, the mean field approach presented earlier would yield the same results, irrespective of  $d$ .

On the other hand, we expect nonlinear effects to be present when the strips become close enough, owing to the correlation between  $s(\mathbf{r}_w)$  and the stress at the boundary,  $\partial_n u(\mathbf{r}_w)$ . Indeed, as can be seen from figure 9, the slippage is increased when the two strips become closer to each other.

This effect, even if only of the order of 10 % in the mass flow rate with respect to the configuration for  $d \gg 1$ , cannot be captured by the previous mean field argument. Notice that a similar sensitivity to the geometrical pattern of the slip and no-slip areas has been reported in the experimental investigation of Ou *et al.* (2004), where it was found that for the same microchannel geometries and shear-free area ratios, micro-ridges aligned along the flow direction consistently outperform regular arrays of microposts. Similar considerations have also been presented by Vinogradova (1999).

## 5. Conclusions

We have presented a mesoscopic model of the fluid–wall interactions which proves capable of reproducing some properties of flows in microchannels. We have defined a suitable implementation of the boundary conditions in a lattice version of the Boltzmann equation describing a single-phase fluid in a microchannel with heterogeneous slippage properties on the surface. In particular, we have shown that it is sufficient to introduce a slip function,  $0 \leq s(\mathbf{r}_w) \leq 1$ , defining the local degree of slip of hydrodynamic fields at the surface, to reproduce qualitatively and, in some cases, even quantitatively, the trends observed either in MD simulations or in some experiments. The function  $s(\mathbf{r}_w)$  plays the role of a renormalizing factor, which incorporates microscopic effects within the mesoscopic description.

We have analysed slip properties in terms of slip length,  $L_s$ , slip velocity,  $V_s$ , pressure drop gain,  $\Pi$  and mass flow rate  $\Phi_s$ , as a function of the degree of slippage, and its spatial localization. The latter parameter is mimicking the degree of roughness of the ultrahydrophobic material in real experiments.

With a proper choice of the slip function  $s(\mathbf{r}_w)$  in longitudinal and transversal configurations, we have reproduced previous analytical results concerning pressure-driven hydrodynamic flows with boundaries made up of alternating strips of zero-slip and infinite-slip (free-shear) lengths (Philip 1972*a, b*; Lauga & Stone 2003). We have also discussed the increment of the slip length in the transition regime, i.e. where the Maxwell-like slip boundary conditions (1.1) are supposed to be replaced by second-order ones (1.2).

The local velocity profile has also been studied with varying Reynolds and Knudsen numbers and the local slip properties on the surface.

The method introduced is able to describe slip lengths of the order of the total height of the channel (of the order of tens of  $\mu\text{m}$ ), or fractions thereof. This is accompanied by an important increase in the mass flow rate, or equivalently, in the pressure drop gain. Whenever possible, we have compared the results based on the heterogeneous LBE with MD simulations and with some recent experiments.

In particular, we have shown that by a suitable choice of bulk viscous properties and surface imposed effects, the H-LBE approach is able to mimic the increase of the slip length as a function of the inverse of the mean pressure in the channel, as observed in recent MD simulations by Cottin-Bizonne *et al.* (2004). Concerning the same MD simulations, we have found a similar linear dependence of the macroscopic slip lengths,  $L_s$  as a function of the microscopic slip properties at the surface. As to the experiments, we have shown that the H-LBE approach is able to achieve semi-quantitative agreement with the experimental study presented in Ou *et al.* (2004), concerning the slip properties as a function of the relative importance of regions with high-slip and low-slip at the surface. The natural application of our numerical tool consists in tuning the free parameters  $s_0$  and  $s_1$  in order to reproduce experimental results in controlled geometries.

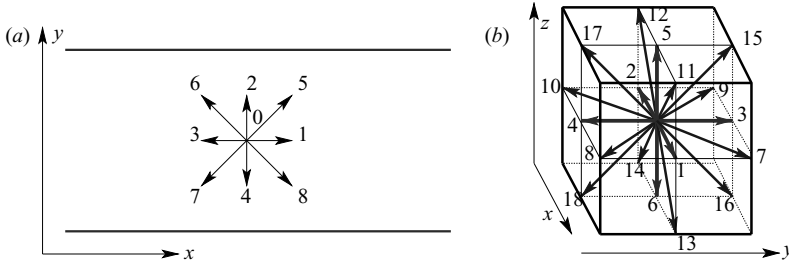


FIGURE 10. (a) Two- and three-dimensional lattice discretization of the velocities in the LBE schemes used in this work. The velocities entering in the north wall in the two-dimensional scheme are  $f_5, f_2, f_6$ . The outgoing velocities are  $f_7, f_4, f_8$ . At the south wall the roles are exchanged.

Then, we can use the LBE scheme with the given  $s_0$  and  $s_1$  values, to explore flows in different geometries and/or with different patterns of the same slip and no-slip materials.

The method is a natural candidate for studying flow properties in more complex geometries, of direct interest for applications. Transport and mixing of active or passive quantities (macromolecules, polymers, etc. . .) can also be addressed.

By definition, the present H-LBE description is limited to a phenomenological interpretation of the slip function. A natural development of this approach, is to implement a multi-phase Boltzmann description, able to account for the wall–fluid interactions and fluid–fluid interactions at a more microscopic level.

This route should open the possibility of discussing the formation of a gas phase close to the wall, induced by the microscopic details of the fluid–wall physics. Results along this direction will be the subject of a forthcoming publication (Benzi *et al.* 2005).

### Appendix A

The lattice Boltzmann equation (LBE) for a pressure-driven channel flow is a stream-and-collide equation involving the particle distribution function  $f_i(\mathbf{x}, t)$  of finding a particle with velocity  $\mathbf{c}_i$  (discrete velocity phase-space) in  $\mathbf{x}$  at time  $t$ . The equation is written in the following form:

$$f_i(\mathbf{r} + \mathbf{c}_i \delta_t, t + \delta_t) - f_i(\mathbf{r}, t) = -\frac{\delta_t}{\tau} (f_i(\mathbf{r}, t) - f_i^{(eq)}(\rho, \mathbf{u})) + \frac{\delta_x}{c^2} F g_l, \quad (\text{A } 1)$$

where  $\tau$  is the relaxation time and  $g_l$  is the projection of the forcing term along  $\mathbf{c}_l$ , with the property

$$\sum_l g_l = 0 \quad \sum_l g_l \mathbf{c}_l = 1. \quad (\text{A } 2)$$

For the case of the two-dimensional grid (2DQ9) depicted in figure 10,  $g_l$  can be taken with the following properties:

$$g_1 = -g_3 \quad g_5 = g_8 = -g_6 = -g_7, \quad (\text{A } 3)$$

leaving only one unknown parameter, say  $g_5$ . Discrete space and time increments are  $\delta_x, \delta_t$ , with  $c = \delta_x / \delta_t$  the intrinsic lattice velocity. The equilibrium distribution

$f_l^{(eq)}(\rho, \mathbf{u})$  is given by:

$$f_l^{(eq)}(\rho, \mathbf{u}) = w_l \rho \left[ 1 + \frac{(\mathbf{c}_l \cdot \mathbf{u})}{c_s^2} + \frac{1}{2} \frac{(\mathbf{c}_l \cdot \mathbf{u})^2}{c_s^4} - \frac{1}{2} \frac{u^2}{c_s^2} \right], \tag{A 4}$$

where  $c_s^2 = c^2/3$  is the sound speed velocity. Concerning the  $2DQ9$  model used here, the velocity phase space is identified by the following discrete set of velocities:

$$\mathbf{c}_\alpha = \begin{cases} \mathbf{c}_0 & = (0, 0)c, \\ \mathbf{c}_1, \mathbf{c}_2, \mathbf{c}_3, \mathbf{c}_4 & = (1, 0)c, (0, 1)c, (-1, 0)c, (0, -1)c, \\ \mathbf{c}_5, \mathbf{c}_6, \mathbf{c}_7, \mathbf{c}_8 & = (1, 1)c, (-1, 1)c, (-1, -1)c, (1, -1)c, \end{cases} \tag{A 5}$$

and the equilibrium weights are  $w_0 = 4/9$ ,  $w_l = 1/9$  for  $l = 1, \dots, 4$ ,  $w_l = 1/36$  for  $l = 5, \dots, 8$ . For the three-dimensional analysis we use a 19-speed model ( $3DQ19$ ) identified by:

$$\mathbf{c}_\alpha = \begin{cases} \mathbf{c}_0 & = (0, 0, 0)c, \\ \mathbf{c}_{1,2}, \mathbf{c}_{3,4}, \mathbf{c}_{5,6} & = (\pm 1, 0, 0)c, (0, \pm 1, 0)c, (0, 0, \pm 1)c, \\ \mathbf{c}_{7,\dots,10}, \mathbf{c}_{11,\dots,14}, \mathbf{c}_{15,\dots,18} & = (\pm 1, \pm 1, 0)c, (\pm 1, 0, \pm 1)c, (0, \pm 1, \pm 1)c, \end{cases} \tag{A 6}$$

and equilibrium weights  $w_0 = 1/3$ ,  $w_l = 1/18$  for  $l = 1, \dots, 6$ ,  $w_l = 1/36$ ,  $l = 8, \dots, 19$ .

The hydrodynamic variables, such as density  $\rho$  and momentum  $\rho \mathbf{u}$ , are moments of the distribution function  $f_l = f_l(\mathbf{x}, t)$ :

$$\rho = \sum_l f_l, \quad \rho \mathbf{u} = \sum_l \mathbf{c}_l f_l, \tag{A 7}$$

and in order to derive hydrodynamic equations from (A 1), we must consider the following expansions:

$$f_l(\mathbf{r} + \mathbf{c}_l \delta_t, t + \delta_t) = \sum_{n=0}^{\infty} \frac{\epsilon^n}{n!} D_t^n f_l(\mathbf{r}, t), \tag{A 8}$$

$$f_l = \sum_{n=0}^{\infty} \epsilon^n f_l^{(n)}, \tag{A 9}$$

$$\partial_t = \sum_{n=0}^{\infty} \epsilon^n \partial_{t_n}, \tag{A 10}$$

where  $\epsilon = \delta_t$  and  $D_t = (\partial_t + \mathbf{c}_l \cdot \nabla)$ .

We can use the expansions (A 8), (A 9), (A 10) in (A 1) and by equating order-by-order in  $\epsilon$ , self-consistent differential constraints on  $f_l^{(n)}$  are obtained.

Up to the first order in  $\epsilon$ , with  $\partial_t = \partial_{t_0} + \epsilon \partial_{t_1}$ , we obtain the following equations:

$$\left. \begin{aligned} \partial_t \rho + \nabla(\rho \mathbf{u}) &= 0, \\ \partial_t \mathbf{u} + (\mathbf{u} \cdot \nabla) \mathbf{u} &= -\frac{1}{\rho} \nabla P + \frac{1}{\rho} \nabla \cdot (\nu \rho \nabla \mathbf{u}), \end{aligned} \right\} \tag{A 11}$$

with  $\nu = ((\tau - 1/2)3)(\delta_x^2/\delta_t)$  and where  $\nabla P$  contains both the imposed mean pressure drop,  $\mathbf{F}$ , and the fluid pressure fluctuations.

### Appendix B

Let us now go back to (A 1), and derive explicitly the non-homogeneous boundary conditions used in (3.3), in the limit  $\delta_x = \delta_t \rightarrow 0$ , with  $c = \delta_x/\delta_t \rightarrow 1$ . We specialize the

discussion to the steady-state boundary condition at the north wall ( $z = L_z$ ) for the two-dimensional lattice (2DQ9):

$$\begin{aligned} f_7(\mathbf{r}_w) &= (1 - s(\mathbf{r}_w))f_5(\mathbf{r}_w) + s(\mathbf{r}_w)f_6(\mathbf{r}_w), \\ f_4(\mathbf{r}_w) &= f_2(\mathbf{r}_w), \\ f_8(\mathbf{r}_w) &= (1 - s(\mathbf{r}_w))f_6(\mathbf{r}_w) + s(\mathbf{r}_w)f_5(\mathbf{r}_w). \end{aligned}$$

Assuming a constant density profile  $\rho = 1$  in the fluid, by definition we have for  $\mathbf{r} = \mathbf{r}_w$ :

$$u_{\parallel}(\mathbf{r}_w) = f_1(\mathbf{r}_w) - f_3(\mathbf{r}_w) + f_5(\mathbf{r}_w) - f_6(\mathbf{r}_w) + f_8(\mathbf{r}_w) - f_7(\mathbf{r}_w). \quad (\text{B } 1)$$

In the limit of small Mach numbers, disregarding all  $O(u^2)$  terms in the equilibrium distribution and using the steady state,  $\partial_t f = 0$ , expansion:

$$f_l(\mathbf{r}) = \sum_{n=0}^{\infty} (-1)^n (\tau(\mathbf{c}_l \nabla))^n [f_l^{(eq)}(\rho, \mathbf{u}) + \tau F_l], \quad (\text{B } 2)$$

we finally obtain the estimate for the slip velocity  $u_{\parallel}$ :

$$\begin{aligned} u_{\parallel}(\mathbf{r}_w) &= 2F\tau g_1 + \frac{2}{3}u_{\parallel}(\mathbf{r}_w) + \frac{2}{3}c^2\tau^2\partial_{\parallel}u_{\parallel}(\mathbf{r}_w) \\ &+ 2s \left[ 2F\tau g_5 + \frac{u_{\parallel}(\mathbf{r}_w)}{6} - \frac{c\tau}{6}\partial_{\parallel}u_{\perp}(\mathbf{r}_w) - \frac{c\tau}{6}\partial_{\perp}u_{\parallel}(\mathbf{r}_w) \right. \\ &\left. + \frac{c^2\tau^2}{6}(\partial_{\parallel}^2 + \partial_{\perp}^2)u_{\parallel}(\mathbf{r}_w) + \frac{c^2\tau^2}{3}\partial_{\parallel}\partial_{\perp}u_{\parallel}(\mathbf{r}_w) \right] + O(\tau^3). \end{aligned} \quad (\text{B } 3)$$

By noticing that the external forcing,  $F$ , is of the order of magnitude of the second-order stress,  $|\partial_{\perp}^2 u_{\parallel}(\mathbf{r}_w)|\nu$ , and  $\nu = c_s^2\tau$ , the first order in  $Kn$  of (A 3) for  $s(\mathbf{r}_w) \neq 1$  reads:

$$\mathbf{u}_{\parallel}(\mathbf{r}_w) = Kn \left( \frac{c}{c_s} \right) \frac{s(\mathbf{r}_w)}{1 - s(\mathbf{r}_w)} |\partial_n \mathbf{u}_{\parallel}(\mathbf{r}_w)|, \quad (\text{B } 4)$$

where we have used  $L_z \partial_{\perp} = \partial_n$ ,  $\tau = L_z Kn / c_s$ ,  $\partial_n \mathbf{u}_{\parallel}(\mathbf{r}_w) = -|\partial_n \mathbf{u}_{\parallel}(\mathbf{r}_w)|$ , which is the expression used in the text. The case  $s(\mathbf{r}_w) = 1$  can be obtained explicitly from (B 3) and results in

$$\partial_{\perp} u_{\parallel}(\mathbf{r}_w) = 2c\tau \partial_{\parallel}^2 u_{\parallel}(\mathbf{r}_w), \quad (\text{B } 5)$$

that, since  $\tau \sim Kn$  is a first order in  $Kn$  relation between the first-order and second-order stress. The second-order calculation in  $Kn$  is particularly simple, if we specialize to a homogeneous case ( $\partial_{\parallel}(\bullet) = 0$ ). After some calculations, we obtain:

$$\mathbf{u}_{\parallel} = Kn \left( \frac{c}{c_s} \right) \frac{s}{1 - s} |\partial_n \mathbf{u}_{\parallel}| + Kn^2 \left( \frac{c}{c_s} \right)^2 (1 - 4g_5) |\partial_n^2 \mathbf{u}_{\parallel}|, \quad (\text{B } 6)$$

which is the second-order, in  $Kn$ , boundary conditions, with unknown parameters  $s$  and  $g_5$  ( $0 \leq g_5 \leq 1/4$ ) used by Sbragaglia & Succi (2005).

#### REFERENCES

- ANSUMALI, S. & KARLIN, I. 2002a Kinetic boundary conditions in the lattice Boltzmann method. *Phys. Rev. E* **66**, 026311.  
 ANSUMALI, S. & KARLIN, I. V. 2002b Entropy function approach to the lattice Boltzmann method. *J. Stat. Phys.* **107**, 291.

- BARRAT, J.-L. & BOCQUET, L. 1999a Influence of wetting properties on hydrodynamic boundary conditions at a fluid/solid interface. *Faraday Discuss.* **112**, 119–127.
- BARRAT, J.-L. & BOCQUET, L. 1999b Large slip effects at a nonwetting fluid solid interface. *Phys. Rev. Lett.* **82**, 4671–4674.
- BATCHELOR, G. 1967 *An Introduction to Fluid Dynamics*. Cambridge University Press.
- BAUDRY, J., CHARLAIX, E., TONCK, A. & MAZUYER, D. 2001 Experimental evidence for a large slip effects at a nonwetting fluid-surface interface. *Langmuir* **17**, 5232.
- BENZI, R., BIFERALE, L., SBRAGAGLIA, M., SUCCI, S. & TOSCHI, F. 2005 Mesoscopic description of the wall-liquid interaction in microchannel flows. In preparation.
- BENZI, R., SUCCI, S. & VERGASSOLA, M. 1992 The lattice Boltzmann equation: theory and applications. *Phys. Rep.* **222**, 145.
- BHATNAGAR, P. L., GROSS, E. & KROOK, M. 1954 A model for collision process in gases. Small amplitude processes in charged and neutral one-component systems. *Phys. Rev.* **94**, 511.
- BICO, J., MARZOLIN, C. & QUÉRÉ, D. 1999 Pearl drops. *Europhys. Lett.* **47**, 220.
- BIRD, G. 1998 *Direct Simulation Monte Carlo*. Oxford University Press.
- BOCQUET, L. & BARRAT, J.-L. 1993 Hydrodynamic boundary conditions and correlation functions of confined fluids. *Phys. Rev. Lett.* **70**, 2726–2729.
- BOGHOSIAN, B., YEPEZ, J., COVENEY, P. V. & WAGNER, A. J. 2001 Theory of the lattice Boltzmann method: dispersion, isotropy, Galilean invariance and stability. *Proc. R. Soc. Lond. A* **457**, 717.
- BONNACURSO, E., BUTT, H. & CRAIG, V. 2003 Surface roughness and hydrodynamic boundary slip of a Newtonian fluid in a completely wetting system. *Phys. Rev. Lett.* **90**, 1445011.
- BONNACURSO, E., KAPPL, M. & BUTT, H. 2002 Hydrodynamic force measurements: boundary slip of water on hydrophilic surfaces and electrokinetic effects. *Phys. Rev. Lett.* **88**, 076130.
- BOON, J. & YIP, S. 1991 *Molecular Hydrodynamics*. Dover.
- CERCIGNANI, C. 1991 *The Mathematical Theory on Non Uniform Gases: an Account of the Kinetic Theory of Viscosity, Thermal Conduction and Diffusion in Gases*. Cambridge University Press.
- CERCIGNANI, C. & DANERI, A. 1963 Flow of rarefied gas between two parallel plates. *J. Appl. Phys.* **34**, 3509.
- CHEN, S. & DOOLEN, G. 1998 Lattice Boltzmann methods for fluid flows. *Annu. Rev. Fluid Mech.* **30**, 329.
- CHEN, W., FADEEV, A., HSIEH, M., ONER, D., YOUNGBLOOD, J. & MCCARTHY, T. 1999 Ultrahydrophobic and ultralyophobic surfaces: some comments and examples. *Langmuir* **15**, 3395.
- CHENG, J.-T. & GIORDANO, N. 2002 Fluid flow through nanometer-scale channels. *Phys. Rev. E* **65**, 0312061.
- CHOI, C., JOHAN, K., WESTIN, A. & BREUER, K. 2003 Apparent slip flows in hydrophilic and hydrophobic microchannels. *Phys. Fluids* **15**, 2897–2902.
- CIEPLAK, M., KOPLIK, J. & BANAVAR, J. 2001 Boundary conditions at a fluid–solid interface. *Phys. Rev. Lett.* **86**, 803–806.
- COTTIN-BIZONNE, C., BARENTINE, C., CHARLAIX, E., BOCQUET, L. & BARRAT, J.-L. 2004 Dynamics of simple liquids at heterogeneous surfaces: molecular dynamics simulations and hydrodynamic description. *Eur. Phys. J. E* **15**, 427–438.
- COTTIN-BIZONNE, C., CHARLAIX, E., BOCQUET, L. & BARRAT, J.-L. 2003 Low friction flows of liquid at nanopatterned interfaces. *Nature Mat.* **2**, 237–240.
- CRAIG, V., NETO, C. & WILLIAMS, D. 2001 Shear-dependent boundary slip in an aqueous Newtonian liquid. *Phys. Rev. Lett.* **87**, 054504(1–4).
- FADEEV, A. & CARNEY, T. M. 1999 Trialkylsilane monolayers covalently attached to silicon surfaces: wettability studies indicating that molecular topography contributes to contact angle hysteresis. *Langmuir* **15**, 3759.
- FRENKEL, D. & SMIT, B. 1995 *Understanding Molecular Simulations. From Algorithms to Applications*. Academic.
- GAD-EL'HAK, M. 1999 The fluid mechanics of microdevices. *Fluid Engng* **121**, 5–33.
- HADJICONSTATINO, N. 2003 Comment on Cercignani's second-order slip coefficient. *Phys. Fluids* **15**, 2352.
- HO, C.-M. & TAI, Y.-C. 1998 Micro-electro-mechanical-systems (mems) and fluid flows. *Annu. Rev. Fluid Mech.* **30**, 579–612.

- KARLIN, I., FERRANTE, A. & OETTINGER, H. 1999 Perfect entropy functions of the lattice Boltzmann method. *Europhys. Lett.* **47**, 182.
- KARNIADAKIS, G. & BENSOKO, A. 2002 *MicroFlows*. Springer.
- KOPLIK, J. & BANAVAR, J. 1991 Continuum deductions from molecular hydrodynamics. *Annu. Rev. Fluid Mech.* **27**, 257.
- KWOK, D. 2003 Discrete Boltzmann equation for microfluidics. *Phys. Rev. Lett.* **90**, 1245021.
- LAUGA, E. & STONE, H. 2003 Effective slip in pressure-driven stokes flow. *J. Fluid. Mech.* **489**, 55.
- LAVALLEE, P., BOON, J. & NOULLEZ, A. 1991 Boundaries in lattice gas flows. *Physica D* **47**, 233.
- LIM, C., SHU, C., NIU, X. & CHEW, Y. 2002 Application of lattice Boltzmann method to simulate microchannel flows. *Phys. Fluids* **14**, 2299–2308.
- LION, N., ROHNER, T., ARNAUD, L. D. I., DAMOC, E., YOUHNOVSKY, N., WU, Z.-Y., ROUSSEL, C., JOSSERAND, J., JENSEN, H., ROSSIER, J., PRZYBYLSKI, M. & GIRAULT, H. 2003 Microfluidics systems in proteomics. *Electrophoresis* **24**, 3533–3562.
- LUM, K., CHANDLER, D. & WEEKS, J. 1999 Hydrophobicity at small and large length scales. *J. Phys. Chem. B* **103**, 4570.
- LUO, L. 1998 The future of lattice-gas and lattice Boltzmann methods. *Workshop on Computational Aerosciences in the 21th Century*, April 22–24.
- LUO, L. 2002 The role of the  $h$  theorem in lattice Boltzmann hydrodynamic simulations. *Rev. Mod. Phys.* **74**, 1203.
- LUO, L. & LALLEMAND, P. 2000 Theory of the lattice Boltzmann method: dispersion, isotropy, Galilean invariance and stability. *Phys. Rev. E* **61**, 6546.
- MCMANAMA, G. & ZANETTI, G. 1998 Use of the Boltzmann equations to simulate lattice-gas automata. *Phys. Rev. Lett.* **61**, 2332.
- MASSEY, B. 1989 *Mechanics of Fluids*. Chapman and Hall.
- MAURER, J., TABELING, P., JOSEPH, P. & WILLAIME, H. 2004 Second order slip laws in microchannels for helium and nitrogen. *Phys. Fluids* **15**, 2613.
- MAXWELL, J. 1879 On stress in rarefied gases arising from inequalities of temperature. *Phil. Trans. R. Soc.* **170**, 231–256.
- NIU, X., SHU, C. & CHEW, Y. 2004 A lattice Boltzmann bgk model for simulation of micro flows. *Europhys. Lett.* **65**, 600.
- ONDA, T., SHIBUCHI, S., SATOH, N. & TSUJII, K. 1996 Superhydrophobic fractal surfaces. *Langmuir* **12**, 2125–2127.
- OU, J., PEROT, B. & ROTHSTEIN, J. 2004 Laminar drag reduction in microchannels using ultrahydrophobic surfaces. *Phys. Fluids* **16**, 4635.
- PHILIP, J. 1972a Flow satisfying mixed no-slip and no-shear conditions. *Z. Angew. Math. Phys.* **23**, 353–370.
- PHILIP, J. 1972b Integral properties of flows satisfying mixed no-slip and no-shear conditions. *Z. Angew. Math. Phys.* **23**, 960–968.
- PIT, R., HERVET, H. & LEGER, L. 2000 Direct experimental evidence of slip in hexadecane: solid interfaces. *Phys. Rev. Lett.* **85**, 980–983.
- PRIEZJEV, N. V., DARHUBER, A. & TROIAN, S. 2004 The slip length of sheared liquid films subject to mixed boundary conditions: comparison between continuum and molecular dynamics simulations. *cond-mat/0405268*.
- RAPAPORT, D. 1995 *The Art of Molecular Dynamics Simulations*. Cambridge University Press.
- SAKURAI, M., TAMAGAWA, H., ARIGA, K., KUNITAKE, T. & INOUE, Y. 1998 Molecular dynamics simulation of water between hydrophobic surfaces. Implications for the long range hydrophobic force. *Chem. Phys. Lett.* **289**, 567.
- SBRAGAGLIA, M. & SUCCI, S. 2005 Analytical calculation of slip flow in lattice Boltzmann models with kinetic boundary conditions. *Phys. Fluids* **17**, 093602.
- SCHWENDEL, D., HAYASHI, T., DAHINT, R., GRUNZE, A. P. M., STEITZ, R. & SCHREIBER, F. 2003 Interaction of water with self-assembled monolayers: neutron reflectivity measurements of the water density in the interface region. *Langmuir* **19**, 2284.
- SHAN, X. & CHEN, H. 1993 Lattice Boltzmann model for simulating flows with multiple phases and components. *Phys. Rev. E* **47**, 1815–1819.
- SHAN, X. & CHEN, H. 1994 Simulation of nonideal gases and liquid–gas transitions by the lattice Boltzmann equation. *Phys. Rev. E* **47**, 2941–2949.
- SUCCI, S. 2001 *The Lattice Boltzmann Equation*. Oxford Science.

- SUCCI, S. 2002 Mesoscopic modeling of slip motion at fluid–solid interfaces with heterogeneous catalysis. *Phys. Rev. Lett.* **89**, 064502.
- SWIFT, M., OSBORN, W. & YEOMANS, J. 1995 Lattice Boltzmann simulations of liquid–gas and binary fluid systems. *Phys. Rev. Lett.* **75**, 830–833.
- TABELING, P. 2003 *Introduction à la microfluidique*. Belin.
- THOMPSON, P. & ROBBINS, M. 1989 Simulations of contact-line motion: slip and the dynamic contact angle. *Phys. Rev. Lett.* **63**, 766–769.
- THOMPSON, P. & ROBBINS, M. 1990 Shear flow near solids: epitaxial order and flow boundary conditions. *Phys. Rev. A* **41**, 6830–6837.
- THOMPSON, P. & TROIAN, S. 1997 General boundary condition for liquid flow at solid surfaces. *Nature* **389**, 360–362.
- TOSCHI, F. & SUCCI, S. 2005 Lattice Boltzmann method at finite Knudsen-number. *Europhys. Lett.* **69**, 549.
- TRETHERWAY, D. & MEINHART, C. 2002 Apparent fluid slip at hydrophobic microchannel walls. *Phys. Fluids* **14**, L9–L12.
- TYRRELL, J. & ATTARD, P. 2001 Images of nanobubbles on hydrophobic surfaces and their interactions. *Phys. Rev. Lett.* **87**, 176104.
- VERBERG, R. & LADD, A. 2000 Lattice-Boltzmann model with sub-grid-scale boundary condition. *Phys. Rev. Lett.* **84**, 2148–2151.
- VERBERG, R., POOLEY, C., YEOMANS, J. & BALAZS, A. 2004 Pattern formation in binary fluids confined between rough, chemically heterogeneous surfaces. *Phys. Rev. Lett.* **93**, 1845011.
- VINOGRADOVA, O. & YABUKOV, G. 2003 Dynamic effects on force measurements. Lubrification and the atomic force microscopy. *Langmuir* **19**, 1227.
- VINOGRANOVA, O. 1999 Slippage of water over hydrophobic surfaces. *Intl J. Miner. Process.* **56**, 31–60.
- WATANABE, K., YANUAR & UDAGAWA, H. 1999 Drag reduction of Newtonian fluid in a circular pipe with a highly water-repellent wall. *J. Fluid Mech.* **381**, 225–238.
- WHITESIDES, G. & STROCK, A. 2001 Flexible methods for microfluids. *Phys. Today* **54**, 42–48.
- WOLF-GLADROW, D. 2000 *Lattice-Gas Cellular Automata and Lattice Boltzmann Models*. Springer.
- ZHANG, X., ZHU, Y. & GRANICK, S. 2002 Hydrophobicity at a janus interface. *Science* **295**, 663–666.
- ZHU, L., TRETHERWAY, D., PETZOLD, L. & MEINHART, C. 2005 Simulation of fluid slip at 3d hydrophobic microchannel walls by the lattice Boltzmann method. *J. Comput. Phys.* **202**, 181–195.
- ZHU, Y. & GRANICK, S. 2001 Rate-dependent slip of newtonian liquid at smooth surfaces. *Phys. Rev. Lett.* **87**, 096105.
- ZHU, Y. & GRANICK, S. 2002 Limits of the hydrodynamic no-slip boundary condition. *Phys. Rev. Lett.* **88**, 106102.